Opto-Electronic Science

ISSN 2097-0382 CN 51-1800/O4

Improved spatiotemporal resolution of anti-scattering super-resolution label-free microscopy via synthetic wave 3D metalens imaging

Yuting Xiao, Lianwei Chen, Mingbo Pu, Mingfeng Xu, Qi Zhang, Yinghui Guo, Tianqu Chen and Xiangang Luo

Citation: Xiao YT, Chen LW, Pu MB, Xu MF, Zhang Q et al. Improved spatiotemporal resolution of anti-scattering super-resolution label-free microscopy via synthetic wave 3D metalens imaging. *Opto-Electron Sci* **2**, 230037 (2023).

https://doi.org/10.29026/oes.2023.230037

Received: 7 October 2023; Accepted: 28 December 2023; Published online: 5 January 2024

Related articles

Dynamic phase assembled terahertz metalens for reversible conversion between linear polarization and arbitrary circular polarization

Jitao Li, Guocui Wang, Zhen Yue, Jingyu Liu, Jie Li, Chenglong Zheng, Yating Zhang, Yan Zhang, Jianquan Yao

Opto-Electronic Advances 2022 **5**, 210062 doi: 10.29026/oea.2022.210062

Physics-data-driven intelligent optimization for large-aperture metalenses

Yingli Ha, Yu Luo, Mingbo Pu, Fei Zhang, Qiong He, Jinjin Jin, Mingfeng Xu, Yinghui Guo, Xiaogang Li, Xiong Li, Xiaoliang Ma, Xiangang Luo

Opto-Electronic Advances 2023 **6**, 230133 doi: 10.29026/oea.2023.230133

Multi-foci metalens for spectra and polarization ellipticity recognition and reconstruction

Hui Gao, Xuhao Fan, Yuxi Wang, Yuncheng Liu, Xinger Wang, Ke Xu, Leimin Deng, Cheng Zeng, Tingan Li, Jinsong Xia, Wei Xiong

Opto-Electronic Science 2023 **2**, 220026 doi: 10.29026/oes.2023.220026

Single-shot mid-infrared incoherent holography using Lucy-Richardson-Rosen algorithm

Vijayakumar Anand, Molong Han, Jovan Maksimovic, Soon Hock Ng, Tomas Katkus, Annaleise Klein, Keith Bambery, Mark J. Tobin, Jitraporn Vongsvivut, Saulius Juodkazis

Opto-Electronic Science 2022 **1**, 210006 doi: 10.29026/oes.2022.210006

More related article in Opto-Electron Journals Group website

Opto-Electronic Science

http://www.oejournal.org/oes

OE_Journal

Website

Opto-Electronic Science

Special Issue on
Digital and Intelligent Optics

Article

November 2023, Vol. 2, No. 11

DOI: 10.29026/oes.2023.230037

Improved spatiotemporal resolution of anti-scattering super-resolution label-free microscopy via synthetic wave 3D metalens imaging

Yuting Xiao[1,2,4†], Lianwei Chen[1,2,3,4†], Mingbo Pu[1,2,3,4*], Mingfeng Xu[1,2,3,4], Qi Zhang[1,2,3,4], Yinghui Guo[1,2,3,4], Tianqu Chen[1,2,4] and Xiangang Luo[1,2,4*]

Super-resolution (SR) microscopy has dramatically enhanced our understanding of biological processes. However, scattering media in thick specimens severely limits the spatial resolution, often rendering the images unclear or indistinguishable. Additionally, live-cell imaging faces challenges in achieving high temporal resolution for fast-moving subcellular structures. Here, we present the principles of a synthetic wave microscopy (SWM) to extract three-dimensional information from thick unlabeled specimens, where photobleaching and phototoxicity are avoided. SWM exploits multiple-wave interferometry to reveal the specimen's phase information in the area of interest, which is not affected by the scattering media in the optical path. SWM achieves ~0.42 λ/NA resolution at an imaging speed of up to 10^6 pixels/s. SWM proves better temporal resolution and sensitivity than the most conventional microscopes currently available while maintaining exceptional SR and anti-scattering capabilities. Penetrating through the scattering media is challenging for conventional imaging techniques. Remarkably, SWM retains its efficacy even in conditions of low signal-to-noise ratios. It facilitates the visualization of dynamic subcellular structures in live cells, encompassing tubular endoplasmic reticulum (ER), lipid droplets, mitochondria, and lysosomes.

Keywords: super-resolution; anti-scattering; unlabeled; high temporal resolution

Xiao YT, Chen LW, Pu MB et al. Improved spatiotemporal resolution of anti-scattering super-resolution label-free microscopy via synthetic wave 3D metalens imaging. *Opto-Electron Sci* **2**, 230037 (2023).

Introduction

Super-resolution (SR) fluorescence microscopy has proved to be an incredible tool to advance science and technology in investigations of cellular or subcellular structures. It has essential applications in disease mechanisms[1–5] and image diagnosis[6–8]. However, live-cell microscopy techniques have long been severely limited because photobleaching and phototoxicity are unavoidable as inherent properties of fluorescence imaging[9–12]. Quantitative phase microscopy (QPM) is a significant

[1]National Key Laboratory of Optical Field Manipulation Science and Technology, Chinese Academy of Sciences, Chengdu 610209, China; [2]State Key Laboratory of Optical Technologies on Nano-Fabrication and Micro-Engineering, Institute of Optics and Electronics, Chinese Academy of Sciences, Chengdu 610209, China; [3]Research Center on Vector Optical Fields, Institute of Optics and Electronics, Chinese Academy of Sciences, Chengdu 610209, China; [4]School of Optoelectronics, University of Chinese Academy of Sciences, Beijing 100049, China.

[†]These authors contributed equally to this work.

*Correspondence: MB Pu, E-mail: pmb@ioe.ac.cn; XG Luo, E-mail: lxg@ioe.ac.cn

Received: 7 October 2023; Accepted: 28 December 2023; Published online: 30 December 2023

advancement in the next generation of label-free imaging[13], provides an alternative solution using refractive index as an endogenous dye, and has gained several significant advancements[14–16].

Imaging through scattering media remains a challenge in optical detection[17–19]. These media, such as biological tissues, do not absorb light significantly; however, they scramble the light path and challenge even low-resolution resolution[18]. The high-contrast super-resolution imaging is mainly limited to imaging depths of 0.1 to 1 μm, such as total internal reflection fluorescence structured illumination microscopy (TIRF-SIM) and grazing incidence structured illumination microscopy (GI-SIM)[20,21]. The resolution and contrast are compromised inside the cell's deep layers[22]. Many approaches have been demonstrated to overcome the scattering effects and enable imaging or focusing capability through scattering media[23–25]. The most direct method is ballistic optical imaging, which filters out the scattered light based on different characteristics, such as Kerr gate[26,27] and confocal microscopy[28–31]. Confocal laser scanning microscopy (CLSM) has been demonstrated highly axial resolution and accurate phase contrast images, and one important milestone and promising frontier development is the Laser oblique scanning optical microscopy (LOSOM)[32]. Recently, laser-scanning gradient light interference microscopy (LS-GLIM) combined differential interference contrast microscopy with CLSM to achieve non-destructively confocal-level depth sectioning, sensitivity, and chemical specificity on unlabeled specimens[33].

However, due to motion artifacts of fast-moving subcellular structures in live cells, most increases in spatial resolution must be matched with an increase in temporal resolution[34]. LS technique and the serial detection of several frames in phase-shifting methods suffer from low throughput, which limits many applications that require high temporal resolution, such as tubular endoplasmic reticulum and neural circuits, due to motion artifacts of fast-moving subcellular structures in live cells. Moreover, the precise imaging of anisotropic structures has remained a challenge for GLIM because two interfering fields are horizontal and vertical. It is worth noticing that many tissues and biological systems contain anisotropic structures[35–37].

In this letter, we present the principles of a label-free anti-scattering imaging method by integrating multiple waves to overcome the above limitation. Here, we have shown that conventional technique avoids photobleaching and phototoxicity in noise-free unlabeled images but fails in authentic microscopic images containing noise. Compared with normal optical imaging[28], we verify that the image quality of synthetic wave microscopy (SWM) has significantly improved, from a blurred image with no clear object features to super-resolution imaging. By exploiting the properties of synthetic waves to vary their phase slowly, the interferometric signal is decoupled from the incoherent, non-modulating background due to multiple scattering. This enables us to penetrate scattering media and successfully image areas of interest. Additionally, SWM shares the capability of numerous scattering suppression with LS-GLIM, delivers 4× faster imaging speed at an imaging speed of up to 10^6 pixels/s, and has a more direct and integrated optical path by abandoning liquid crystal modulators. Moreover, SWM is unaffected by tissue polarization information and can achieve polarization-insensitive imaging. By introducing metalens, we demonstrate the SWM with the lateral resolution of 0.42 λ/NA. Therefore, our SWM can improve current anti-scattering techniques to push their spatiotemporal resolution limits and better resolve intricate, 3D, and fast dynamics in live cells.

Metawave imaging model

Theoretical derivation

The essence of our approach is based on the fact when two light waves with tiny wavelength differences transmit through the scattering media, the phase delay introduced by the scattering media is almost the same. Based on this, we design one technique with two closely positioned focused light waves to detect the material property at the focal point but ignoring the influence of the scattering media in its optical paths. (See Supplementary Section 1 for more information). The optical path and image processing are presented in Fig. 1(a) and 1(b). The synthetic wave source generation module comprises two laser scanning devices and a beam splitter. The amplitude of two input electric fields is equal to A. The frequencies of two input electric fields are ω_1 and ω_2, respectively. The initial phase of two input electric fields are φ_1 and φ_2, respectively. After combination, they form a synthetic wave pulse:

$$\begin{aligned} E(t) =& A\mathrm{e}^{\mathrm{i}(\omega_1 t+\varphi_1)}+A\mathrm{e}^{\mathrm{i}(\omega_2 t+\varphi_2)} \\ =& 2A\cos\left[(\Delta\omega t+\Delta\varphi)/2\right]\mathrm{e}^{\mathrm{i}(\overline{\omega}t+\overline{\varphi})}\,, \end{aligned} \tag{1}$$

where $\Delta\omega$ and $\Delta\varphi$ are the frequency difference and phase difference of the two sources, respectively, $\overline{\omega}$ and $\overline{\varphi}$ are

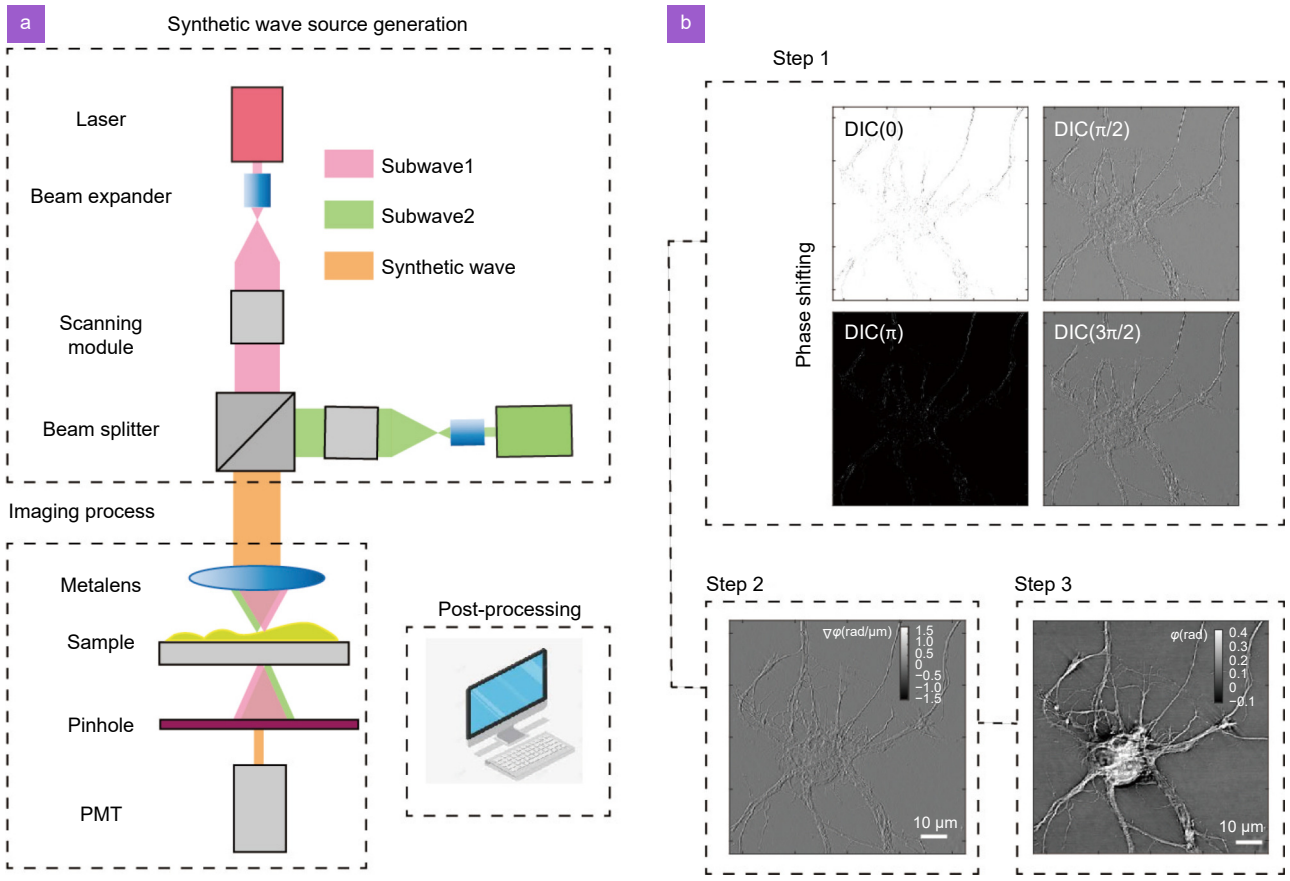

Fig. 1 | (**a**) The SWM system configuration comprises four main components: a synthetic wave source generation module, a metalens, a pinhole, and a PMT. (**b**) The schematic diagram of the post-processing process. The first row is the four phase-shifting frames. The second row is the reconstructed quantitative phase gradient image. The third row is the reconstructed quantitative phase image.

the average frequency and phase of the two sources, respectively. The superimposed of two simple harmonics with little frequency difference allows us to enlarge the harmonics period from femtoseconds to picoseconds. Considering that the photomultiplier tube (PMT) already has accuracy at the picosecond level, the PMT can accurately record the synthesized wave's envelope intensity changes. It should be noted that the picosecond period is not the limitation of this technique. The period can be flexibly tuned by changing the frequencies of the two synthetic waves. Picosecond period is chosen to balance the performance of the detector and the scanning speed.

$$\begin{aligned} I(\boldsymbol{r},t) &= \left\langle |E(\boldsymbol{r},t)|^2 \right\rangle \\ &= 2A^2\left[1+\cos\left((\Delta\omega t+\Delta\varphi(\boldsymbol{r}))\right)\right] , \end{aligned} \tag{2}$$

where $\boldsymbol{r}$ denotes the pixels in the sample, $\Delta\varphi(\boldsymbol{r})$ denotes the phase difference between the two waves.

In this case, the phase image $\Delta\varphi(\boldsymbol{r})$ is determined from four intensity measurements corresponding to $t=0, T/4, T/2, 3T/4$, termed as four-step phase-measuring method. Here, T denotes the envelope period of the synthetic wave. It should be noted that for a more general case, more points in the harmonic period can be chosen to improve the accuracy of the phase detection:

$$\begin{aligned} \Delta\varphi(\boldsymbol{r}) =& \arg\{[I(\boldsymbol{r},3T/4)-I(\boldsymbol{r},T/4)], \\ & [I(\boldsymbol{r},T/2)-I(\boldsymbol{r},0)]\} . \end{aligned} \tag{3}$$

We used the shear distance value $\delta\boldsymbol{r}$, greater than or equal to the focal spot size.

$$\Delta\varphi(\boldsymbol{r}) = \varphi(\boldsymbol{r}+\delta\boldsymbol{r})-\varphi(\boldsymbol{r}) \approx \nabla_r\varphi(\boldsymbol{r})\delta\boldsymbol{r} , \tag{4}$$

where $\nabla_r\varphi(\boldsymbol{r})$ denotes the phase gradient along the $\boldsymbol{r}$ direction at a point $\boldsymbol{r}$ on the sample.

Now we convert the coordinate system to a cartesian coordinate system for data post-processing. We obtain the phase gradient along the direction of the shear (x-direction):

$$\nabla_x\varphi(x,y) = \frac{\varphi(x+\delta x,y)-\varphi(x,y)}{\delta x} , \tag{5}$$

where (x,y) denotes the pixels in the sample, δx denotes shear distance value along the x direction.

To integrate the measured phase map, we perform a

cumulative sum along the direction of the shear direction:

$$\varphi(x,y)=\int_0^x[\nabla_x\varphi(x',y)]\mathrm{d}x'+\varphi(0,y)\ , \tag{6}$$

where $\varphi(0,y)$ is the initial value, which is obtained with some prior knowledge of the specimen. For example, if $(0,y)$ is a background location, the phase $\varphi(0,y)$ should be set to 0 radians (See Supplementary Section 2 for more information).

When imaged in a transmission configuration, the expected phase shift from a phase step object is

$$\varphi(x,y)=\frac{2\pi}{\lambda}n(x,y)d(x,y)\ , \tag{7}$$

where λ is the wavelength of the illumination, $n(x,y)$ is the refractive index, and $d(x,y)$ is the height. The wavelengths of the two sub-waves are nearly identical, so we refer to λ as 1064 nm. In modern laser technology, high-stability lasers can achieve highly narrow linewidths in the sub-hertz range[38,39], and the corresponding wavelength linewidth ($\Delta\lambda$) can be converted to less than 10^{-20} m using the formula $\Delta\lambda=\Delta v\cdot\lambda^2/c$. This allows us to use two lasers with minimal wavelength differences.

The design of SWM

Figure 1(a) illustrates the SWM system configuration, which comprises four main components: a synthetic wave source generation module, a metalens, a pinhole, and a PMT. The synthetic wave source generation module consists of two collimated continuous-wave (CW) lasers, two laser scanning modules and a beam splitter. Two CW lasers at 1064 nm and 1064.1 nm pass through the beam splitter and are focused by a metalens. For the imaging of bio samples, the laser power needs to be controlled to avoid damaging the samples, which is chosen to be ~1 mW. The scanning modules control the light source with different tilt angles to generate different beam shear distance values on the sample, the sample is placed at the focal plane of metalens. The pinhole is placed at twice the focal length of the metalens, and the size is chosen to be 40 μm. Then, the light source passes through a pinhole and is recorded by PMT with ps-level detection time accuracy (See Supplementary Section 6 for more information). In our experiments, each point of the sample is scanned over a total time length of $\Delta t_1=10^{-6}$ s (the speed of the scanning module) with a step size of $\Delta t_2=10^{-12}$ s (the rate of PMT), so imaging speed reaches 10^6 pixel/s ($\frac{1}{\Delta t_1}$). In this condition, the limiting factor is the capability of the scanning module. It is possible to achieve ~10^{11} pixels/s ($>\frac{1}{4\Delta t_2}$) imaging if the scanning module's speed is further increased to match the rate of the PMT. Therefore, SWM is a suitable technique for observing living cells over long periods, in large areas, and with high temporal resolution. As shown in Fig. 1(b), four differential interference phase contrast (DIC) frames are used to reconstruct the quantitative phase image in post-processing. We obtain the phase gradient diagram using Eq. (3) with the four intensity maps provided. By utilizing the provided phase gradient, we integrate along the gradient direction using Eq. (6) to obtain the phase value. Notably, employing a greater number of frames enhances phase reconstruction accuracy (See Supplementary Section 2 for more information).

The Abbe diffraction limit refers to the minimum resolution distance expressed by $\lambda/2NA$[40]. Rayleigh further pointed out that the Rayleigh criterion for physical two-point resolution is 1 Airy spot ($0.61\lambda/NA$)[41]. Consequently, the minimum distance that a focusing imaging system can resolve is nearly the radius of the Airy spot, which is the focal spot size of the optical system. Compared with the traditional optical lens, the metalens is much more attractive due to its distinct advantages of powerful focusing capabilities[42–48]. Hence, we design a metalens to achieve super-resolution imaging. Si and Al_2O_3 are used considering large-area fabrication feasibility and their common usage in near-infrared (NIR) light. As shown in Fig. 2(a), the meta-atom comprises a Si nanopillar and a rectangular lattice Al_2O_3 substrate. Considering fabrication feasibility, the nanopillar height was chosen to be 700 nm. Then, we calculate the amplitude and phase delay of meta-atom using rigorous coupled wave analysis (RCWA) solver RETICOLO. As shown in Fig. 2(b) and Fig. 2(c), Lattice constant ranges from 400 to 700 nm to avoid higher order diffraction and duty cycle ranges from 0 to 1. As shown in Fig. 2(d), when we choose a constant period of $P=500$ nm, the transmission efficiency is close to 100% and full 2π phase coverage is achieved as the width changes from 100 to 320 nm. After scanning the unit cell structure, we arrange the meta-atoms based on the ideal phase profiles. The calculated ideal phase profile of the designed metalens is shown in Fig. 2(e) and the schematic of designed metalens operating in transmission mode is shown in Fig. 2(f). The next step involves utilizing

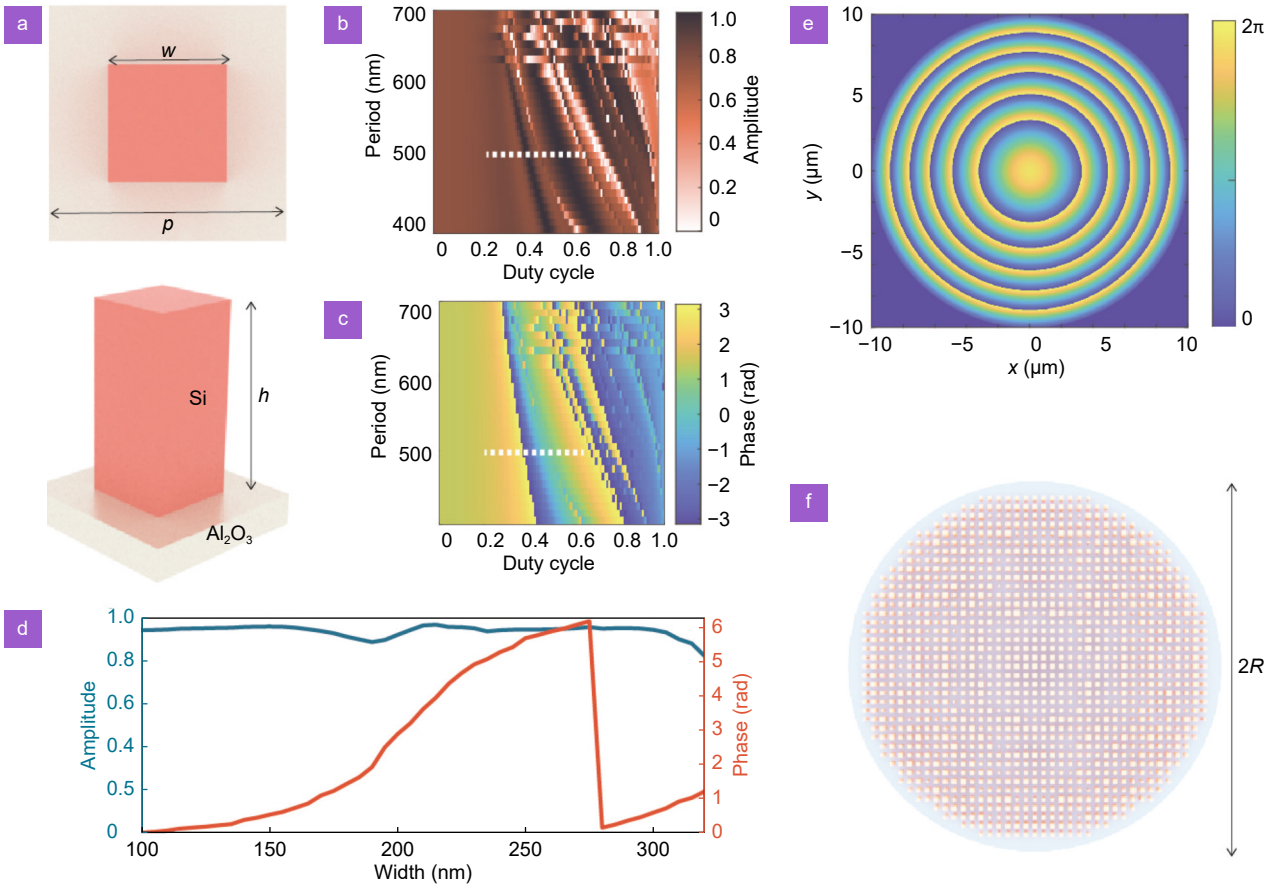

Fig. 2 | (**a**) The unit cell of the metalens is shown from both a top view and a side view. (**b**) The transmission coefficient's amplitude and (**c**) its phase delay for square lattice periodic nanopillar transmit arrays as a function of duty cycles of the nanopillars and the lattice constant. The square lattice period of 500 nm is indicated by a white dashed line. (**d**) The amplitude and phase of the transmission coefficient with a fixed lattice constant of 500 nm while varying the width of the nanopillars. (**e**) The calculated phase profile. (**f**) The schematic of metalens operating in transmission mode.

techniques such as super-oscillatory lenses[49] or microspheres[50–52] to further enhance the resolution, which is beyond the scope of this work. We investigate the influence of different size for metalens performance. (See Supplementary Section 3 for more information)

Results and discussion

Resolution investigation

A commercial electromagnetic software (Lumerical FDTD solutions) analyzes electromagnetic properties based on the finite-difference time-domain method. In the simulations, the cutoff of convergence accuracy is set as 10^{-6}. Considering rapidly changing spatial profiles and the feasible computation time, a medium size aperture of 20 μm (about 19λ) is chosen as the computation time increases significantly with the increment of metalens size. A commercial electromagnetic software (Lumerical FDTD solutions) analyzes electromagnetic properties based on the finite-difference time-domain method. In the simulations, the cutoff of convergence accuracy is set as 10^{-6}. To achieve high spatial resolution, a focal length of 5 μm is chosen (*NA* = 0.89). The parameters in the text are designed for verifying the concept. However, metalens with a diameter of 2 inches is entirely feasible in actual production, has been demonstrated image qualities comparable to a state-of-the-art commercial objective[43]. Note that, theoretically with the introduction of the scanning galvanometers (scanning angle of ±11 degrees) and the fabricated metalens (focal length of 200 mm), SWM would have an imaging field of 1224 mm^2. This can be further extended if the sample is mounted on a mechanical translational stage that can further shift the imaging area.

The focusing characteristics of metalens are characterized in detail. We start from the light incident in a normal direction. Figure 3(a) shows the normalized intensity distribution in the *x*-*y* plane and the 1D distribution

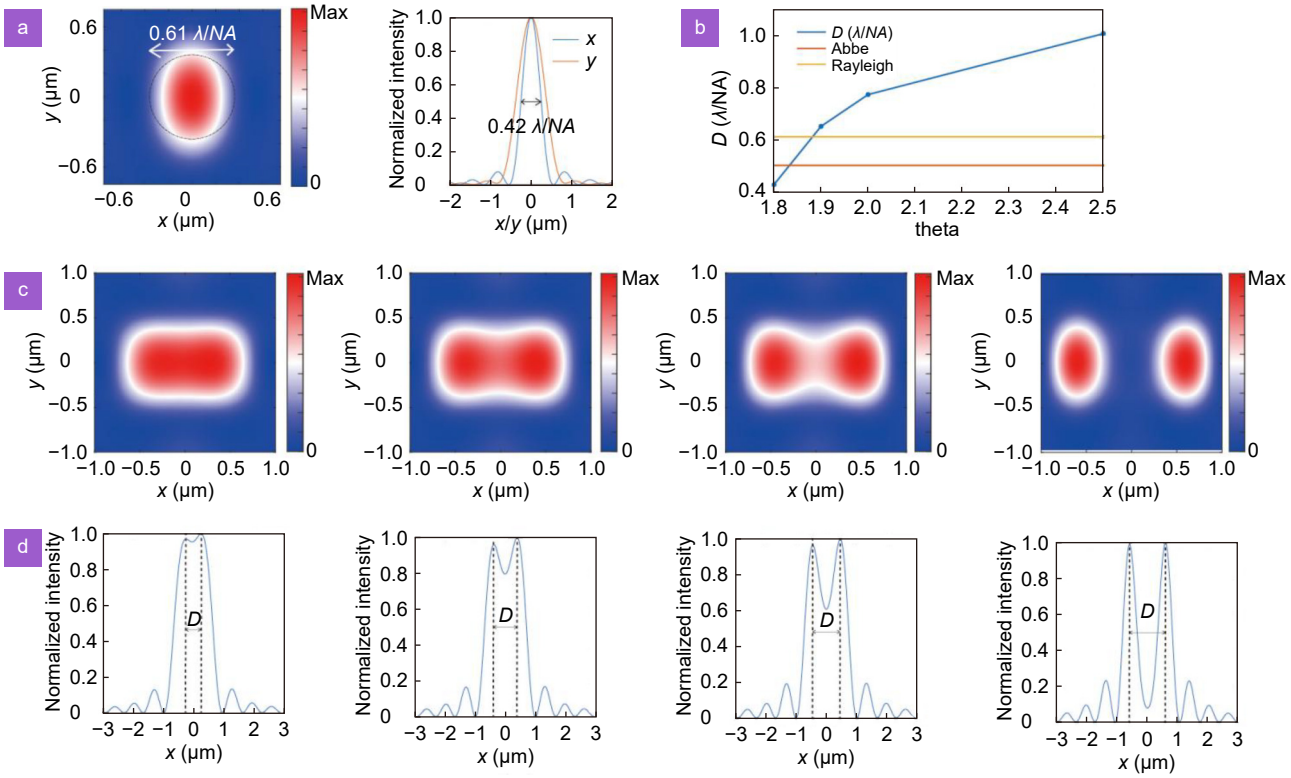

Fig. 3 | (**a**) Normalized intensity distribution when metawave source is incident normally. The first row is 2D distribution. The dotted line indicates the Airy spot area. The second row is 1D distribution along the *x*- and *y*-direction. The arrow indicates the FWHM of focus spot. (**b**) Lateral resolution as a function of incident angles. (**c**) Normalized intensity profiles of the focal spot for different incident angles *x*-*y* plane. (**d**) Normalized intensity distribution along the *x*-direction in the *x*-*y* plane when metawave source is incident with different angles. The arrow represents the resolution of the SWM. The incident angles are 2.5°, 2°, 1.9° and 1.8°, respectively. *D* represents the distance between the centers of two focused light spots.

along the *x*- and *y*-direction. The full width at half maximum (FWHM) along the *x*-direction is 0.42 λ/NA due to the intensity of the sidelobe increases, leading to the super-diffraction focusing phenomenon along the *x*-direction, which is due to its remarkable ability to manipulate electromagnetic waves at subwavelength dimensions[52–54]. Figure 3(b) shows lateral resolution as a function of incident angles. In theory, the minimum resolution of SWM is achieved when the distance between the centers of the two focal spots is nearly equal to FWHM. Figure 3(c) presents the normalized intensity distribution in the *x*-*y* plane. Figure 3(d) presents the normalized intensity distribution in the 1D distribution along the *x*-direction. The synthetic wave source incident angles are 2.5°, 2°, 1.9° and 1.8°, respectively. It confirmed that the SWM achieves a super-resolution of 0.42 λ/NA when the metalens is illuminated by two *x*-polarized plane waves with incident angles of ±1.8°.

Anti-scattering capability investigation

We test the anti-scattering capability by changing complexity of the scattering media and the dielectric layer distance from the sample. Firstly, we reconstruct phase without scattering media. The ideal phase difference ranges over 2π radians with a step size of 0.25π radians ($\Delta\varphi_{\text{ideal}}(i) = i * \frac{\pi}{4}, i = 0, 1, \ldots 7$). Figure 4(a) presents the normalized intensity curve recorded by PMT during one synthetic wave period for different ideal phase differences. Secondly, we establish a model for imaging through a scattering dielectric layer (Fig. 4(b)). On the left-hand side, the abrupt phase of the scattering phase plane is set to the maximum phase multiplied by a random number (0~1). It represents a scattering media with totally random distribution and full period phase disturbance, which stands for the worst imaging conditions for most cases. We change the complexity of the scattering media by varying the maximum phase. Figure 4(c) shows the reconstruction results ($\Delta\varphi_{\text{test}}(i), i = 0, 1, \ldots 7$) when scattering media layer in the same focal distances. The reconstruction results closely match the real values represented by the red lines, when the maximum phase is

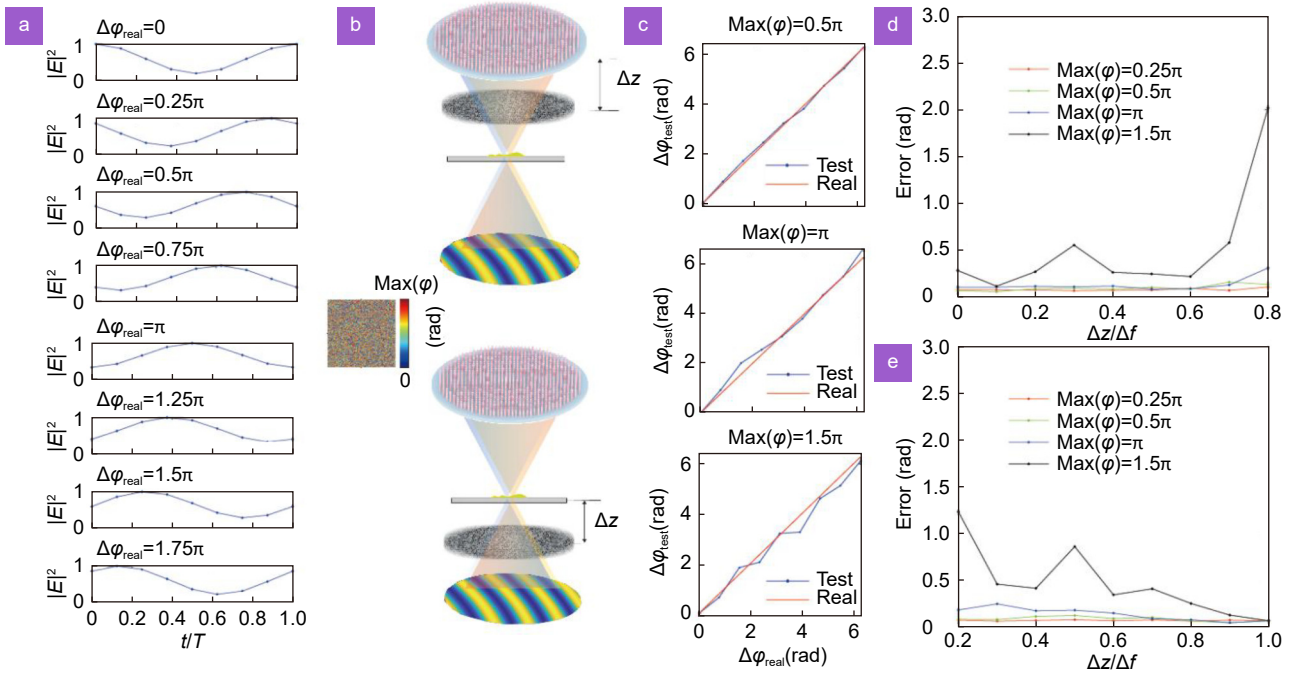

Fig. 4 | (**a**) Normalized intensity curve recorded by PMT during one period for different phase differences. (**b**) The top section represents an anti-scattering imaging model with a medium screen positioned above the imaged object, while the bottom section depicts an anti-scattering imaging model with a medium screen placed below the imaged object. On the left-hand side, there is a map illustrating the distribution of the scattering media's phase. (**c**) Reconstruction phase difference vs. real phase difference. (**d**) Detection error as it varies with the distance of the scattering medium screen from the metalens, with the medium screen located above the imaged object. (**e**) Detection error as it varies with the distance of the scattering medium screen from the sample, with the medium screen situated below the imaged object.

0.5π. Even when the maximum phase is π, there is only a minor discrepancy. It means that SWM can generate high-contrast images and are not affected by the scatter in the optical path. The reconstruction results deviate from the real values when the maximum phase is 1.5π. This phenomenon is due to less ballistic light and more multiple-scattered light reach the ideal focus point as the maximum phase increases.

Next, we assess the impact both of complexity of the scattering media and the dielectric layer distance from the sample. We establish a criterion to evaluate the anti-scattering capability of SWM, which is calculated as the average measurement error between the reconstructed phase and the ideal phase $error = \dfrac{\sum_i \left|\varphi_{\text{ideal}}(i) - \varphi_{\text{test}}(i)\right|}{8}$. In Fig. 4(d) and 4(e) , it can be observed that as the scattering phase screen gets closer to the specimen, the error increases. This phenomenon occurs due to the reduction in the overlap area between the two beams. Even when the maximum interference phase is equal to 0.5π, the average error of different distance is less than 0.1 radians. In this case, it is possible to image the target object clearly (as demonstrated in Fig. 5). The anti-scattering capability achieved with the SWM is directly related to two effects. First, the wavelengths of the two sub-waves are nearly identical. Secondly, the two interference fields are also nearly identical except for a small transverse shift in spatial. Consequently, the two fields suffer equal degradation, and interferometry remains unchanged. We conduct an additional simulation to further demonstrate the capability of the proposed method under a realistic optical condition (See Supplementary Section 4 for more information).

Imaging result

We compare the temporal resolution of LS-GLIM and SWM. The acquisition time of each frame depends on the dwell time and pixel numbers set for the image acquisition. Given an image case with the same acquisition time of ~1 s and the same dwell time of 1 μs/pixel: In LS-GLIM, we obtain an image with 500 × 500 pixels for 1 frame. In SWM, we obtain an image with 1000 × 1000 pixels for 1 frame. As shown in Fig 5(a), we image a neuron cell without the scattering layer using LS-GLIM and SWM, respectively. The temporal resolution of SWM surpasses that of LS-GLIM, and SWM offers a

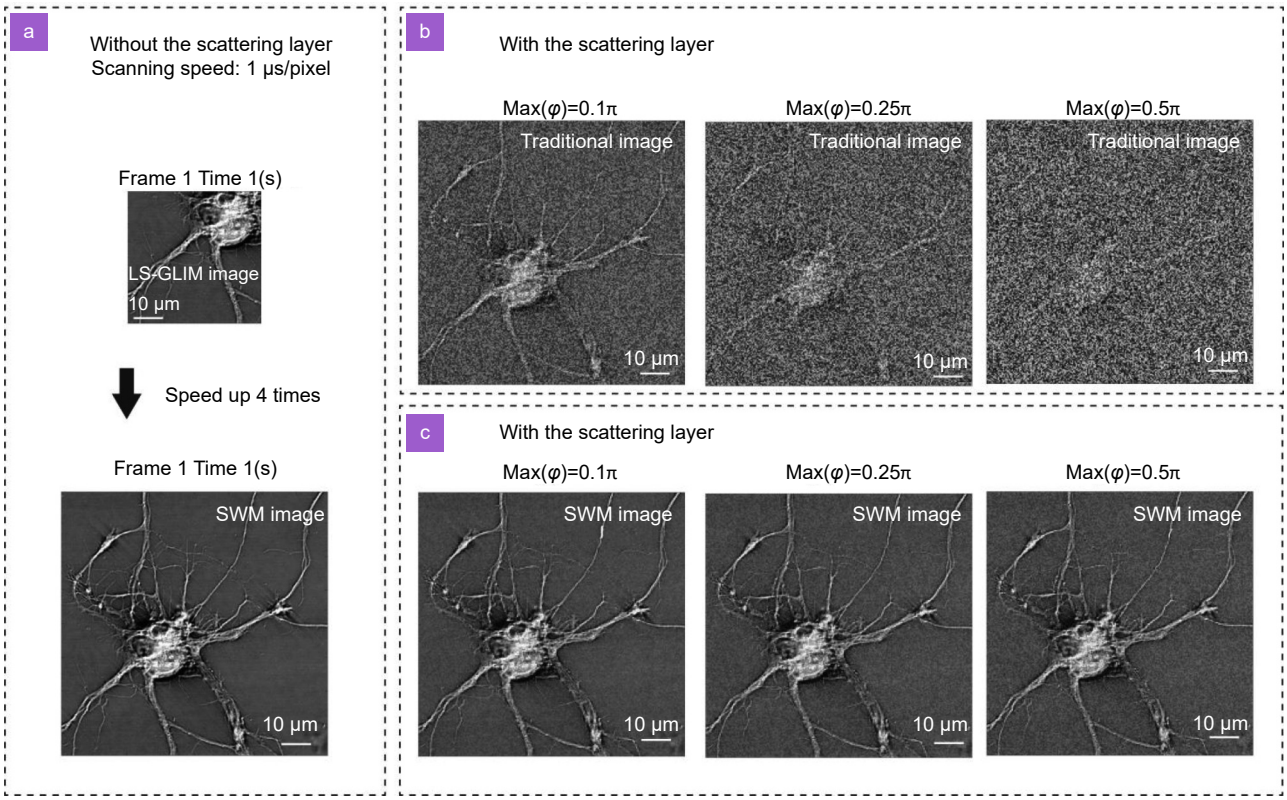

Fig. 5 | (**a**) LS-GLIM image and SWM image taken without the scattering layer. (**b**) traditional image taken with the scattering layer. (**c**) SWM image taken with the scattering layer.

fourfold greater field of view compared to LS-GLIM. This phenomenon occurs due to LS-GLIM needs the liquid crystal to modulate the phase shift between the two orthogonal polarizations after each intensity frame is recorded[32] and SWM abandons liquid crystal modulators by leveraging the temporal variation of intensity in synthesized waves.

We image a neuron cell over a 90 μm×90 μm field of view to compare the anti-scattering capability of traditional QPM[13] and SWM. It is important to note that we did not actually perform experimental tests with biological samples, but rather used data from the literature[13] for imaging comparisons for proof-of-concept of the superiority of our imaging. Conducting imaging experiments on biological samples is the next step in our work, and all sample preparation procedures involving animals need to be reviewed and approved by the ministry of health. The scattering layer maximum phase is set to 0.1π, 0.25π and 0.5π, respectively. SWM could achieve anti-scattering imaging because the two interfering fields are almost identical except for a small transverse spatial shift. The two fields suffer equal degradation due to multiple scattering, so interferometry remains unchanged, thus allowing it to resolve high-quality images with greater depth and accuracy compared to traditional imaging techniques. As shown in Fig. 5(b), at a maximum phase ~0.1π, a substantial fraction of the light has been scattered, resulting in a blurry background, obscuring the object features. At a maximum phase of ~0.5π, essentially all of the light has been scattered, and the conventional image degrades to the point where no sharp object features can be seen. As depicted in Fig. 5(c), SWM allows for clear visualization of the nucleolus and the dendrites of the neuron cell. Supplementary Video 1 and Section 7 illustrate the anti-scattering capability of SWM on unlabeled dynamic neurons for 10 s time-lapse imaging. The SWM image records the dynamic changes of neuronal cells and does not suffer from scattering medium, phototoxicity, or photobleaching while maintaining a super-resolution image with high contrast. As a result, SWM is suitable for the non-destructive study of living cellular systems over long periods of time. We make a comprehensive comparison among 5 different optical imaging techniques in spatial resolution, temporal resolution, live-cell compatibility, and anti-scattering capability level. (See Supplementary Section 5 for more information)

Conclusions

In summary, we present a label-free anti-scattering imaging method by the integration of multiple waves. In comparison to the most advanced QPW techniques, SWM excels in extending the temporal resolution and is not influenced by polarization information. Under the same measurement time, SWM enables a fourfold expansion of the imaged field of view. Most importantly, SWM exhibits superior anti-scattering performance in comparison to traditional QPW techniques, such that it resolves high-quality images with greater depth and accuracy. We anticipate that SWM can be potentially adopted at a broad scale because a SW source generation module can be readily added to many existing microscopy systems, such as structured illumination microscopy and confocal microscopy. We hope that the results presented here can serve as an important step toward the field of optical detection, which has significant implications for various fields, including medical imaging, industrial inspection, and scientific research.

References

1. Nixon-Abell J, Obara CJ, Weigel AV, Li D, Legant WR et al. Increased spatiotemporal resolution reveals highly dynamic dense tubular matrices in the peripheral ER. *Science* **354**, aaf3928 (2016).
2. Bourzac K. Cell imaging: beyond the limits. *Nature* **526**, S50–S54 (2015).
3. Cheng PH, Pu KY. Molecular imaging and disease theranostics with renal-clearable optical agents. *Nat Rev Mater* **6**, 1095–1113 (2021).
4. Huang YY, Yu MX, Zheng J. Proximal tubules eliminate endocytosed gold nanoparticles through an organelle-extrusion-mediated self-renewal mechanism. *Nat Nanotechnol* **18**, 637–646 (2023).
5. Yamanaka Y, Hamidi S, Yoshioka-Kobayashi K, Munira S, Sunadome K et al. Reconstituting human somitogenesis in vitro. *Nature* **614**, 509–520 (2023).
6. Etzioni R, Urban N, Ramsey S, McIntosh M, Schwartz S et al. The case for early detection. *Nat Rev Cancer* **3**, 243–252 (2003).
7. Freedman BS, Brooks CR, Lam AQ, Fu HX, Morizane R et al. Modelling kidney disease with CRISPR-mutant kidney organoids derived from human pluripotent epiblast spheroids. *Nat Commun* **6**, 8715 (2015).
8. Monteil V, Kwon H, Prado P, Hagelkrüys A, Wimmer RA et al. Inhibition of SARS-CoV-2 infections in engineered human tissues using clinical-grade soluble human ACE2. *Cell* **181**, 905–913.e7 (2020).
9. Huang XS, Fan JC, Li LJ, Liu HS, Wu RL et al. Fast, long-term, super-resolution imaging with Hessian structured illumination microscopy. *Nat Biotechnol* **36**, 451–459 (2018).
10. Laissue PP, Alghamdi RA, Tomancak P, Reynaud EG, Shroff H. Assessing phototoxicity in live fluorescence imaging. *Nat Methods* **14**, 657–661 (2017).
11. Tamamitsu M, Toda K, Shimada H, Honda T, Takarada M et al. Label-free biochemical quantitative phase imaging with mid-infrared photothermal effect. *Optica* **7**, 359–366 (2020).
12. Fu PC, Cao WL, Chen TR, Huang XJ, Le TR et al. Super-resolution imaging of non-fluorescent molecules by photothermal relaxation localization microscopy. *Nat Photonics* **17**, 330–337 (2023).
13. Park Y, Depeursinge C, Popescu G. Quantitative phase imaging in biomedicine. *Nat Photonics* **12**, 578–589 (2018).
14. Kandel ME, Hu CF, Naseri Kouzehgarani G, Min E, Sullivan KM et al. Epi-illumination gradient light interference microscopy for imaging opaque structures. *Nat Commun* **10**, 4691 (2019).
15. Nguyen TH, Kandel ME, Rubessa M, Wheeler MB, Popescu G. Gradient light interference microscopy for 3D imaging of unlabeled specimens. *Nat Commun* **8**, 210 (2017).
16. Kandel ME, Teng KW, Selvin PR, Popescu G. Label-free imaging of single microtubule dynamics using spatial light interference microscopy. *ACS Nano* **11**, 647–655 (2017).
17. Bertolotti J, Katz O. Imaging in complex media. *Nat Phys* **18**, 1008–1017 (2022).
18. Rotter S, Gigan S. Light fields in complex media: mesoscopic scattering meets wave control. *Rev Mod Phys* **89**, 015005 (2017).
19. Yoon S, Kim M, Jang M, Choi Y, Choi W et al. Deep optical imaging within complex scattering media. *Nat Rev Phys* **2**, 141–158 (2020).
20. Guo YT, Li D, Zhang SW, Yang YR, Liu JJ et al. Visualizing intracellular organelle and cytoskeletal interactions at nanoscale resolution on millisecond timescales. *Cell* **175**, 1430–1442.e17 (2018).
21. Li D, Shao L, Chen BC, Zhang X, Zhang MS et al. Extended-resolution structured illumination imaging of endocytic and cytoskeletal dynamics. *Science* **349**, aab3500 (2015).
22. Kang S, Kang P, Jeong S, Kwon Y, Yang TD et al. High-resolution adaptive optical imaging within thick scattering media using closed-loop accumulation of single scattering. *Nat Commun* **8**, 2157 (2017).
23. Bertolotti J, van Putten EG, Blum C, Lagendijk A, Vos WL et al. Non-invasive imaging through opaque scattering layers. *Nature* **491**, 232–234 (2012).
24. Hernandez O, Papagiakoumou E, Tanese D, Fidelin K, Wyart C et al. Three-dimensional spatiotemporal focusing of holographic patterns. *Nat Commun* **7**, 11928 (2016).
25. Liu RH, Sun Y, Zhu JB, Tian L, Kamilov US. Recovery of continuous 3D refractive index maps from discrete intensity-only measurements using neural fields. *Nat Mach Intell* **4**, 781–791 (2022).
26. Redo-Sanchez A, Heshmat B, Aghasi A, Naqvi S, Zhang MJ et al. Terahertz time-gated spectral imaging for content extraction through layered structures. *Nat Commun* **7**, 12665 (2016).
27. Wang L, Ho PP, Liu C, Zhang G, Alfano RR. Ballistic 2-D imaging through scattering walls using an ultrafast optical Kerr gate. *Science* **253**, 769–771 (1991).
28. Huff J. The Airyscan detector from ZEISS: confocal imaging with improved signal-to-noise ratio and super-resolution. *Nat Methods* **12**, i–ii (2015).
29. Wang JF, Yang M, Yang L, Zhang Y, Yuan J et al. A confocal endoscope for cellular imaging. *Engineering* **1**, 351–360 (2015).
30. Singh VR, Yang YA, Yu H, Kamm RD, Yaqoob Z et al. Studying

nucleic envelope and plasma membrane mechanics of eukaryotic cells using confocal reflectance interferometric microscopy. *Nat Commun* **10**, 3652 (2019).
31. Jonkman J, Brown CM, Wright GD, Anderson KI, North AJ. Tutorial: guidance for quantitative confocal microscopy. *Nat Protoc* **15**, 1585–1611 (2020).
32. Ding YC, Xie H, Peng T, Lu YQ, Jin DY et al. Laser oblique scanning optical microscopy (LOSOM) for phase relief imaging. *Opt Express* **20**, 14100–14108 (2012).
33. Chen X, Kandel ME, He SH, Hu CF, Lee YJ et al. Artificial confocal microscopy for deep label-free imaging. *Nat Photonics* **17**, 250–258 (2023).
34. Zhao WS, Zhao SQ, Li LJ, Huang XS, Xing SJ et al. Sparse deconvolution improves the resolution of live-cell super-resolution fluorescence microscopy. *Nat Biotechnol* **40**, 606–617 (2022).
35. Chen SQ, Xie ZQ, Ye HP, Wang XR, Guo ZH et al. Cylindrical vector beam multiplexer/demultiplexer using off-axis polarization control. *Light Sci Appl* **10**, 222 (2021).
36. Shribak M, Inoué S. Orientation-independent differential interference contrast microscopy. *Appl Opt* **45**, 460–469 (2006).
37. Gurjar RS, Backman V, Perelman LT, Georgakoudi I, Badizadegan K et al. Imaging human epithelial properties with polarized light-scattering spectroscopy. *Nat Med* **7**, 1245–1248 (2001).
38. Liu J, Liu T, Chen L, Zhang LB, Xu GJ et al. A compact sub-hertz linewidth Fabry Perot cavity frequency stabilized laser for space application. *Opt Laser Technol* **136**, 106777 (2021).
39. Gundavarapu S, Brodnik GM, Puckett M, Huffman T, Bose D et al. Sub-hertz fundamental linewidth photonic integrated Brillouin laser. *Nat Photonics* **13**, 60–67 (2019).
40. Abbe E. Beiträge zur Theorie des Mikroskops und der mikroskopischen Wahrnehmung. *Arch Mikrosk Anat* **9**, 413–468 (1873).
41. Airy GB. On the diffraction of an object-glass with circular aperture. *Trans Cambridge Philos Soc* **5**, 283 (1835).
42. Sang D, Xu MF, Pu MB, Zhang F, Guo YH et al. Toward high-efficiency ultrahigh numerical aperture freeform metalens: from vector diffraction theory to topology optimization. *Laser Photonics Rev* **16**, 2200265 (2022).
43. Khorasaninejad M, Chen WT, Devlin RC, Oh J, Zhu AY et al. Metalenses at visible wavelengths: Diffraction-limited focusing and subwavelength resolution imaging. *Science* **352**, 1190–1194 (2016).
44. Luo XG. Subwavelength artificial structures: opening a new era for engineering optics. *Adv Mater* **31**, 1804680 (2019).
45. Luo XG. Engineering optics 2.0: a revolution in optical materials, devices, and systems. *ACS Photonics* **5**, 4724–4738 (2018).
46. Li JT, Wang GC, Yue Z, Liu JY, Li J et al. Dynamic phase assembled terahertz metalens for reversible conversion between linear polarization and arbitrary circular polarization. *Opto-Electron Adv* **5**, 210062 (2022).
47. Gao H, Fan XH, Wang YX, Liu YC, Wang XG et al. Multi-foci metalens for spectra and polarization ellipticity recognition and reconstruction. Opto-Electron Sci. **2**, 220026 (2023).
48. Ha YL, Luo Y, Pu MB, Zhang F, He Q et al. Physics-data-driven intelligent optimization for large-aperture metalenses. *Opto-Electron Adv* **6**, 230133 (2023).
49. Huang K, Ye HP, Teng JH, Yeo SP, Luk'yanchuk B et al. Optimization-free superoscillatory lens using phase and amplitude masks. *Laser Photonics Rev* **8**, 152–157 (2014).
50. Wu GX, Zhou Y, Hong MH. Sub-50 nm optical imaging in ambient air with 10× objective lens enabled by hyper-hemi-microsphere. *Light Sci Appl* **12**, 49 (2023).
51. Zhou Y, Hong MH. Realization of noncontact confocal optical microsphere imaging microscope. *Microsc Res Tech* **84**, 2381–2387 (2021).
52. Chen LW, Zhou Y, Li Y, Hong MH. Microsphere enhanced optical imaging and patterning: from physics to applications. *Appl Phys Rev* **6**, 021304 (2019).
53. Luo XG. Principles of electromagnetic waves in metasurfaces. Sci. China Phys. *Mech. Astron* **58**, 594201 (2015).
54. Luo XG. Multiscale optical field manipulation via planar digital optics. *ACS Photonics* **10**, 2116–2127 (2023).

Acknowledgements

We are grateful for financial support from CAS West Light Grant (xbzg-zdsys-202206) and National Key Research and Development Program of China (2021YFA1401003).

Author contributions

YT Xiao refined methodology, performed simulations, and write original draft. LW Chen proposed the original idea and supervised the project. MB Pu and XG Luo participated in idea discussions that shaped the objectives of the paper. MF Xu, Q Zhang, and YH Guo provided detailed proofreading and editing for the manuscript, ensuring its language fluency and structural clarity. TQ Chen revised the figures to present experimental results and data in a more visually intuitive manner.

Competing interests

The authors declare no competing financial interests.

Supplementary information

Supplementary information for this paper is available.
https://doi.org/10.29026/oes.2023.230037